

Geophysical Research Letters

RESEARCH LETTER

10.1029/2018GL081364

Key Points:

- Earthquake rupture initiated on the shallow part of the fault, then ruptured toward the surface and on deeper parts of the fault
- Coseismic slip occurs at greater depths than do the aftershocks and the vast majority of regional seismicity
- Pore fluids may have influenced the earthquake nucleation and shallow slip, but are unlikely to have influenced deep rupture

Supporting Information:

- Supporting Information S1

Correspondence to:

M. P. Moschetti,
mmoschetti@usgs.gov

Citation:

Moschetti, M. P., Hartzell, S. H., & Herrmann, R. B. (2019). Rupture model of the M5.8 Pawnee, Oklahoma, earthquake from regional and teleseismic waveforms. *Geophysical Research Letters*, 46, 2494–2502. <https://doi.org/10.1029/2018GL081364>



Received 17 NOV 2018

Accepted 12 FEB 2019

Accepted article online 15 FEB 2019

Published online 7 MAR 2019

Rupture Model of the M5.8 Pawnee, Oklahoma, Earthquake From Regional and Teleseismic Waveforms

M. P. Moschetti¹ , S. H. Hartzell¹ , and R. B. Herrmann²

¹U.S. Geological Survey, Denver, CO, USA, ²Department of Earth and Atmospheric Sciences, St. Louis University, St. Louis, MO, USA

Abstract The 2016 M5.8 Pawnee, Oklahoma, earthquake is the largest earthquake to have been induced by wastewater disposal. We infer the coseismic slip history from analysis of apparent source time functions and inversion of regional and teleseismic *P* waveforms, using aftershocks as empirical Green's functions. The earthquake nucleated on the shallow part of the fault, initially rupturing toward the surface, followed shortly thereafter by slip deeper on the fault. Deeper slip occurred below the aftershocks and at greater depths than most induced seismicity in the region, suggesting that small- to moderate-sized earthquakes may not occur on deeper parts of faults in Oklahoma because they are further from failure than shallower fault sections. Comparisons with models of pore pressure perturbations further suggest that the earthquake may have initiated within a region of higher pore pressure perturbation but was not confined to this zone. These observations inform source physics and understanding of maximum magnitudes.

Plain Language Summary We analyzed seismic recordings from the 2016 M5.8 Pawnee, Oklahoma, earthquake to examine how the earthquake ruptured in time and how slip occurred on different parts of the fault. Our results show that the earthquake started on the shallow part of the fault, followed by slip toward the surface and slip occurring on the deeper part of the fault. By comparing our results with a previous study of changes in pore fluid pressures caused by injection, we find that the earthquake may have started where pore pressures were affected, but that the earthquake process continued outside of this region. That earthquake rupture can extend outside of the areas directly affected by injection processes is important for understanding maximum magnitudes from induced earthquakes.

1. Introduction

The 3 September 2016 12:02:44 (UTC) M5.8 earthquake near Pawnee, Oklahoma, ruptured the previously unmapped, northwest-striking Sooner Lake fault and was the largest historically recorded earthquake in the state, exposing more than 70 k people to strong ground shaking, and causing light damage to structures in the vicinity (Clayton et al., 2016; U.S. Geological Survey PAGER, 2018; Yeck et al., 2017; Figure 1). Numerous studies point to the injection of produced wastewater associated with oil and gas operations as a critical causative factor for the earthquake (e.g., Chen et al., 2017; McGarr & Barbour, 2017; Yeck et al., 2017). The earthquake is part of an unprecedented increase in seismicity rates in Oklahoma of more than two orders of magnitude compared to historical rates, owing to induced earthquakes (Ellsworth, 2013; Keranen et al., 2014; Llenos & Michael, 2013; Moschetti et al., 2016). While the rate increase of induced earthquakes across North America has followed a similar trend, the largest magnitude earthquakes, to date, have occurred in Oklahoma. As a consequence, the forecasted short-term (1-year) seismic hazard in Oklahoma has been the highest of any state in the central and eastern United States for the past several years (Petersen et al., 2016, 2017, 2018).

Deep wastewater injection is the predominant cause of induced earthquakes in Oklahoma, and the general mechanism is well understood (Ellsworth, 2013; Healy et al., 1970; Raleigh et al., 1976; Weingarten et al., 2015). Rupture on critically stressed faults that are preferentially oriented in the current regional stress field may be induced by increasing pore pressures, which decrease the effective normal stresses, thereby reducing fault strength (Alt & Zoback, 2016). Poroelastic effects also contribute to the on-fault Coulomb failure stresses, particularly when injection is far from the fault zone, and may have also contributed to the Pawnee

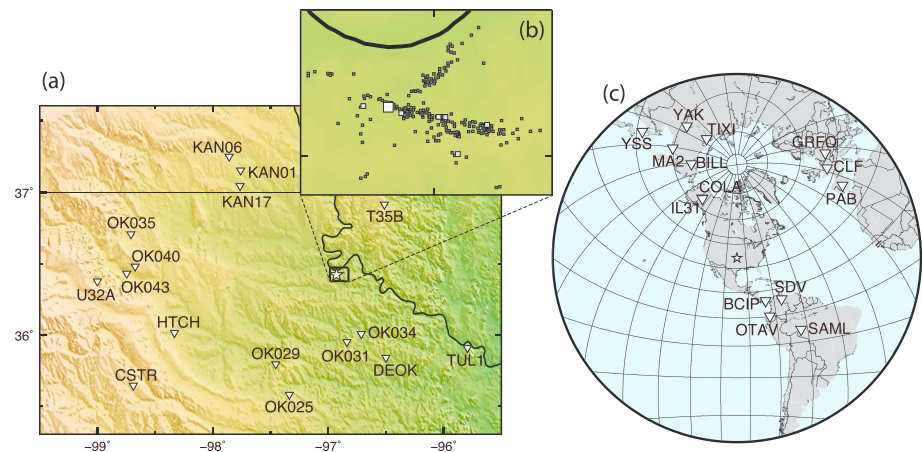


Figure 1. Seismic station and earthquake locations. (a) Locations of regional stations (triangles) relative to the epicenter location of the 2016 **M**5.8 Pawnee earthquake. Dashed lines depict the boundaries of the inset map. (b) Locations of relocated earthquakes from Yeck et al. (2017). Mainshock and aftershock epicenter locations are plotted as larger and smaller open squares, respectively. (c) Distribution of stations used in the teleseismic inversion.

earthquake rupture (Barbour et al., 2017; Segall & Lu, 2015), but its contribution to the earthquake rupture is not considered here.

Coseismic slip models of the Pawnee earthquake have been previously developed from InSAR (Fielding et al., 2017); InSAR and GPS data (Pollitz et al., 2017); and InSAR, regional, and teleseismic data with frequencies up to 0.5 Hz (Grandin et al., 2017). While the resulting slip models find that most slip occurred east, and primarily downdip, of the hypocenter, there are discrepancies in the depths over which coseismic slip occurred (supporting information Text S1). In addition, the geodetic and lower-frequency nature of the seismic data of these inversions preclude the ability to resolve whether additional slip complexity exists for this event, as has been found for other induced earthquakes in Oklahoma (e.g., López-Comino & Cesca, 2018; Sun & Hartzell, 2014).

In this study, we compute and analyze apparent source time functions (ASTFs) and invert regional and teleseismic *P* waveforms from the Pawnee, Oklahoma, earthquake to produce a consistent model of the spatial and temporal evolution of the rupture process.

2. Data and Methods

2.1. Seismic Waveform Data

The rupture model of the Pawnee earthquake is derived from ASTF analysis, using regional *P* waveforms, and from a finite-fault inversion, using regional and teleseismic *P* waveforms. ASTF analysis employs vertical-component records from stations within 300 km from the GS, N4, TA, and U.S. networks. Records are high-pass filtered with a corner frequency of 0.1 Hz, and *P* waveforms are windowed from 1 s before to 5 s after the first arrival. Regional waveforms for the finite-fault inversion are selected from 16 stations located about 50–185 km from the mainshock (Figure 1 and Table S1). The three-component waveforms are band-pass filtered (0.5–3 Hz) and sampled at a period of 0.025 s. Because earthquake aftershock records are used as the Green's functions in the ASTF and finite-fault inversions (Hartzell, 1978), we do not correct for the effects of the instrument response. Aftershocks are selected for proximity to the fault plane, existence of or ability to estimate seismic moment from regional waveform modeling, and agreement of focal mechanisms with that of the mainshock (Table S2). Vertical-component teleseismic waveforms are collected from 14 stations ($31^{\circ} \leq \Delta \leq 81^{\circ}$) with good azimuthal coverage (Figure 1). In this distance range, *P* waves have simple paths through the mantle and avoid upper-mantle triplication features, which are present at distances less than about 29° . Rather than deconvolving the instrument response from the earthquake records, we convolved the synthetics with the appropriate instrument response. This approach has previously been used to minimize the introduction of low-frequency noise into the time series data (Hartzell

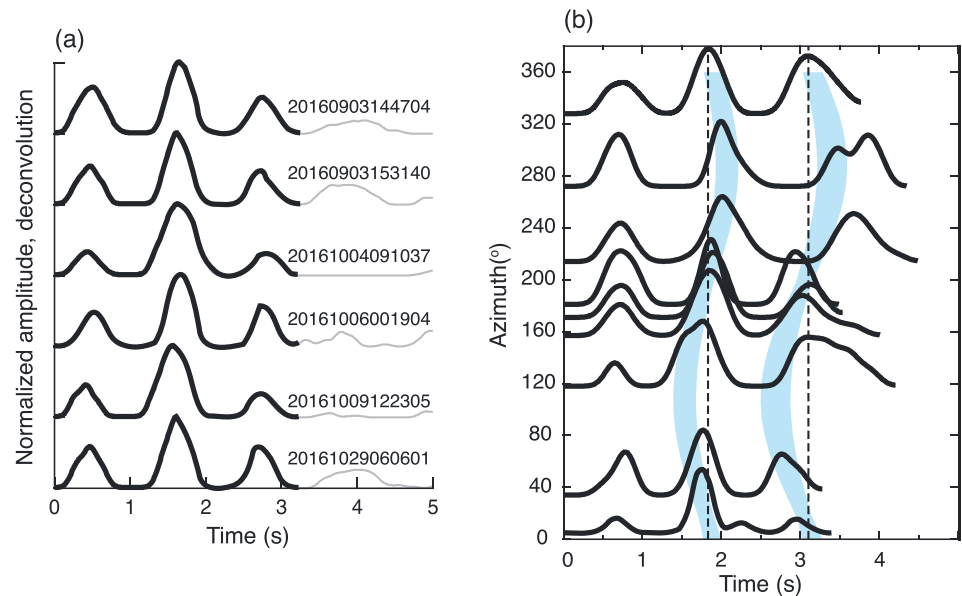


Figure 2. Example waveform deconvolutions and apparent source time functions. (a) Deconvolutions of the mainshock record with aftershock records from station GSOK031. (b) Apparent source time functions are plotted as a function of azimuth (black lines) and compared with theoretical delay times (equation (1)), modeled for a range of rupture delay times, and epicentral distances between the hypocenter and the subevent centroids (blue curves).

et al., 2013; Sun & Hartzell, 2014). No other filtering is performed to preserve waveform details. Records were sampled at a period of 0.02 s.

As evidenced by example waveforms (Figure S1), regional wave propagation imparts a complicated ground motion response. Comparison of the extended durations of multiple phases between the mainshock and aftershock records suggests that structural features give rise to the late-arriving phases of these records. For the finite-fault inversion, durations of 5 s from the initial phase arrivals were used for the regional and teleseismic records. This duration encompasses the rupture duration computed by the Global Centroid Moment Tensor project ($t_{D-half} = 1.8$ s; Dziewonski et al., 1981; Ekström et al., 2012) and minimizes the potential for mapping structural effects into the source solution.

2.2. ASTFs and Centroid Arrival Times

Investigation of the source complexity of the Pawnee earthquake proceeds by deconvolving aftershock records from the mainshock records to form ASTFs. ASTFs vary as a function of station azimuth due to wave propagation and finite-source effects. However, they contain information about the temporal evolution of the earthquake source, including the relative timing and moments of distinct patches of moment release.

Waveform deconvolutions are computed by an iterative time-domain method (Ligorria & Ammon, 1999), which enforces positivity and uses a smoothing parameter that corresponds to low-pass filtering with a corner frequency of about 2 Hz. Example deconvolutions from station GSOK031 and six selected earthquake aftershocks are plotted in Figure 2a. At times less than about 3 s, the deconvolution waveforms strongly agree, and we attribute the complexity to finite-fault effects. Beyond about 3 s, there are significant differences in the waveforms, with several records exhibiting no signal and two records exhibiting a longer-period and lower-amplitude feature. We interpret these later-arriving features to structural artifacts or other noise, which may result from differing depths and locations of the aftershocks, and only model the first three pulses. Other stations exhibit similar features from the use of different aftershock records, and we therefore choose a single aftershock record—M3.4, 9 October 2016, 12:23:05 UTC—to form the set of ASTFs. This event is selected because it is the largest magnitude aftershock, thereby providing better signal at farther stations, which resulted in improved resolution with azimuth.

To guide analysis of the ASTFs, we calculate the dependence of theoretical centroid arrival times on azimuth, assuming azimuthal variations to be caused by horizontal offset of the subevents from the hypocenter (e.g., López-Comino & Cesca, 2018). For a vertical fault:

$$\tau_i = \Delta t_i - \frac{d_j}{V_p} \cos(\phi - \beta_i), \quad (1)$$

where τ_i is the apparent time of centroid i ; Δt_i and d_j are the rupture delay time and epicentral distance between the hypocenter and the centroid of a subevent, respectively; V_p is the P wave speed; and ϕ and β_i are the azimuths to the station and the subevent, respectively, with respect to the hypocenter.

2.3. Inversion for Earthquake Rupture Model

Kinematic earthquake rupture is inverted on a fault plane consistent with the regional moment tensor solution, with fault strike, dip, and rake values of 288° , 88° , and 0° , respectively (U.S. Geological Survey, 2016). Fault dimensions were chosen to exceed the expected rupture dimensions for a **M**5.8 earthquake—14 km along-strike and 7 km downdip, with the top of the fault plane at 3 km depth. Rupture modeling assumes the 5.6-km-deep hypocenter location from Yeck et al. (2017) and specifies 0.5-by-0.5 km² subfaults, with 28 along-strike and 14 downdip.

We use adjusted aftershocks (Hartzell, 1978) and synthetic seismograms from generalized ray theory (Helmberger, 1983) for the subfault Green's functions modeling the regional and teleseismic records, respectively. Aftershock records were processed as follows to allow their use as empirical Green's functions in the inversion: Record amplitudes were scaled to normalize the seismic moments of all events to a common value, subfault Green's functions were constructed from the scaled aftershock records by identifying the closest available event, scaling the amplitudes to account for far-field geometric attenuation, and shifting the initiation time of the subevent Green's functions by assuming a constant rupture velocity ($V_{rup} = 2.5, 2.7$ km/s; Table S3). In this way, we use aftershocks located off the fault surface. Moment magnitude of all aftershocks are computed from long-period waveform modeling with a regional seismic velocity model (Herrmann et al., 2011; Table S2). We do not adjust the aftershock waveforms to account for expected variations in amplitudes due to depth variations, which represent one source of epistemic uncertainty in the source models.

The inversion permits subfault slip, \mathbf{x} , in five successive 0.2-s time windows (Hartzell & Heaton, 1983) and is regularized with smoothing, \mathbf{S} , and moment-minimization, \mathbf{M} , constraints.

$$\begin{bmatrix} \mathbf{C}_d^{-1} \mathbf{A} \\ \lambda_1 \mathbf{S} \\ \lambda_2 \mathbf{M} \end{bmatrix} \mathbf{x} = \begin{bmatrix} \mathbf{C}_d^{-1} \mathbf{b} \\ 0 \\ 0 \end{bmatrix}, \quad (2)$$

where \mathbf{A} and \mathbf{b} consist of the subfault Green's functions and the waveform data, respectively. Tikhonov weights ($\lambda = \lambda_1 = \lambda_2$) for regularizing the calculation employ the values optimized by Mendoza and Hartzell (2013) from L-curve analysis, which minimizes the trade-offs between data misfit and satisfying the inversion constraints (Hansen, 2005). A diagonal data covariance matrix, \mathbf{C}_d , normalizes the amplitudes of the waveform data so that all records have similar weights in the inversion. The slip solution is solved by a nonnegative least-squares algorithm (Lawson & Hanson, 1974). Although the inversion employs a constant rupture speed, the multiwindow approach allows for small deviations of the rupture speed from the assumed values, as well as variations in the rise time over which slip accumulates once rupture initiates. A fundamental issue in the inversion of the regional and teleseismic waveforms for the Pawnee slip model was the low signal-to-noise levels of the first-arriving seismic phases of the regional aftershocks and of all teleseismic records. The solution permitted small waveform shifts to optimize alignment of mainshock records through a nonlinear inversion (Liu et al., 1995; Text S2).

3. Results

3.1. ASTF Analysis

Three main pulses manifest in the ASTFs, which we interpret as three subevents of the earthquake rupture (Figure 2b). From the relative amplitudes of the pulses, subevent 2, corresponding to the second pulse, has a

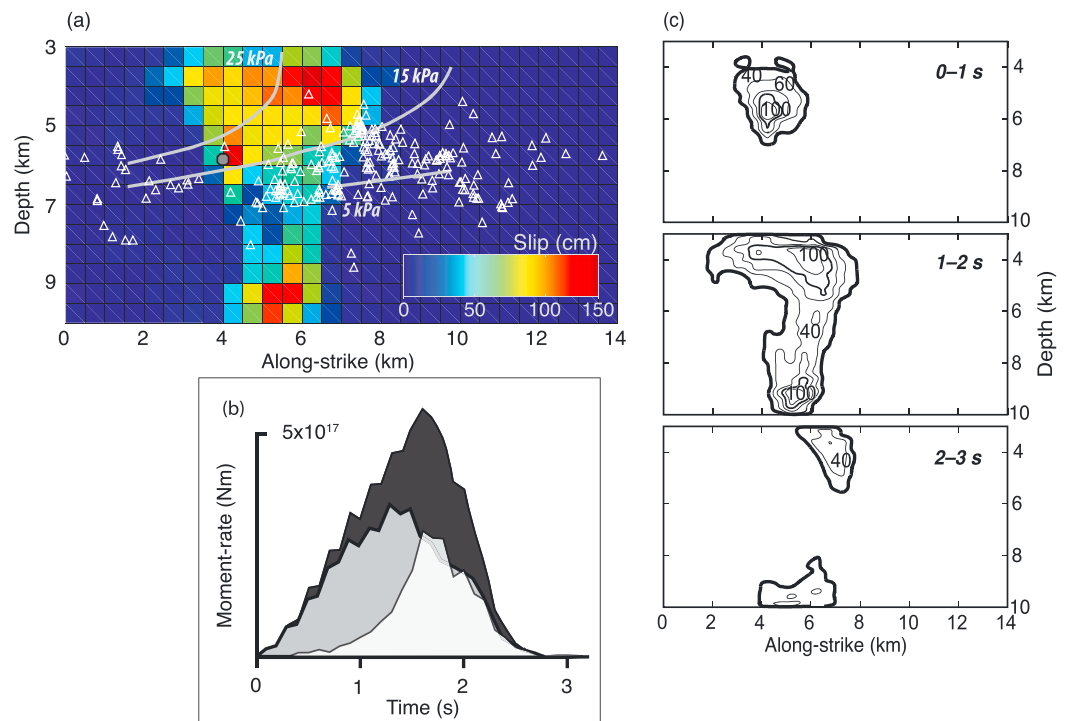


Figure 3. Slip model, moment rate function, and time evolution of the rupture. (a) Slip model from the joint inversion of regional and teleseismic P waveforms. The earthquake hypocenter is depicted by the white circle. Earthquake aftershocks from Yeck et al. (2017) are depicted by white triangles. Gray lines depict on-fault pore pressure contours from Barbour et al. (2017) for the time immediately before the $M_{5.8}$ earthquake. (b) The total moment rate function (dark gray) is plotted with the contributions from the shallower fault (<7 km; gray) and deeper fault (white). (c) Time progression of the earthquake rupture is depicted in three, 1-s windows.

larger seismic moment than subevent 1 (first pulse) or subevent 3 (third pulse). The azimuthal dependence of subevents 2 and 3 suggests that they were horizontally offset from the hypocenter location. Centroid arrival times of subevent 2 exhibit clear azimuthal dependence, and the centroid arrival times of subevent 3 indicate a similar azimuthal dependence, though the variations contain further signal complications or noise.

We compute theoretical centroid arrival times (equation (1)) to infer the spatial separation and time-delay between rupture of subevents 1, 2, and 3. The fault is presumed to be vertically dipping, with P wave speeds of 5.5 km/s, and subevents are prescribed to be located along the strike of the fault. Errors in the P wave speed map directly into errors in the horizontal offset of the subevents. Subevent 1 is interpreted to correspond to seismic moment release at the hypocenter because of the small time delays of the first pulses in the ASTFs; waveforms are aligned on the first pulse, and peak amplitudes are normalized.

Forward modeling identifies time delays and horizontal centroid separations for subevents 2 and 3, relative to subevent 1, that reproduce the azimuthal variations of the ASTFs (Figure 2b). Distances from the hypocenter to the subevent centroids are computed from the time delays by assuming a range of rupture speeds ($V_{rup} = 2.5\text{--}2.7$ km/s). Seismic moment release from subevent 2 occurs 1–1.2 s after subevent 1, and the subevent is horizontally offset by 1.25–1.75 km (total separation of 2.5–3.2 km). Seismic moment release from subevent 3 occurs 2.3–2.5 s after subevent 1, and the subevent is horizontally offset by 1.5–2.5 km (total distance of 5.8–6.8 km). The phase agreement in the azimuthal variations of centroidal delay times indicates that the azimuths from the hypocenter to subevents 2 and 3 are similar. Given the assumed strike of the fault (288°), subevents 2 and 3 are inferred to be located ESE of the hypocenter within 1.25 to 2.5 km along-strike from the hypocenter, with the inferred total distances suggesting that the subevents are vertically offset from the hypocenter (1.8–2.9 and 5.2–6.6 km, respectively).

3.2. Finite-Fault Rupture Model

The finite-fault rupture model is derived from the joint inversion of regional and teleseismic data and from a constant rupture speed of 2.7 km/s (Figure 3). Waveform fits are depicted in Figures S2–S4. The results are robust with respect to use of only regional seismic data (Text S3 and Figure S5), as well as to variation of the constant rupture speed (Text S3 and Figure S6). The seismic data do not permit resolution of spatially varying rupture speeds.

Rupture modeling indicates that the left-lateral strike-slip earthquake released seismic moment across a region measuring about $8 \times 7 \text{ km}^2$ (Figure 3a). Slip was largely confined to spatially separated regions that are shallower and deeper than the hypocenter. The regional and teleseismic data are explained by coseismic slip confined to the crystalline basement. Three regions of higher slip ($>100 \text{ cm}$) occurred—near the hypocenter, on the shallower part of the fault, and deeper on the fault. Shallower ($<7 \text{ km}$) and deeper slip have moments of 4.49×10^{17} and $2.29 \times 10^{17} \text{ Nm}$, respectively.

The finite-fault slip model exhibits good agreement with the observations and modeling results from the ASTFs. The potential locations for subevents 2 and 3, computed from the range of delay times and along-strike distances derived from ASTF modeling, agree reasonably with the regions of high slip from the finite-fault inversion (Figure S7). We do not expect perfect matches between the spatial distributions because the ASTFs do not account for differences in the waveforms from source depth or variations along the fault. However, the identification of three subevents in the ASTFs, which generally match the spatial locations and timing indicated by the finite-fault source model, support the rupture model of the finite-fault inversion.

The average stress drop computed across the fault surface, for regions with nonzero slip, is 4 MPa (Okada, 1985), with locally higher values in regions of high slip (Figure S8). Total stress drop exhibits little sensitivity to rupture speed, with stress drop estimates from $V_{\text{rup}} = 2.5$ and 2.7 km/s differing by less than 2%. Detailed analyses of the spatial variations of stress drop are likely beyond the resolution of the inversion.

The seismic moment rate function and windowed time-histories of the slip model indicate that rupture initiated at 5.6 km and ruptured toward the surface, followed by a secondary rupture of the deeper slip patch (Figures 3a–3c). In the initial phase of the rupture, slip occurred predominantly at shallower depths. Rupture of the deeper patch initiated about 0.5–1 s after the earthquake nucleation, with the moment rate maximum from the deeper patch occurring shortly after that of the shallower patch. Following rupture initiation on the deeper patch, shallower and deeper parts of the fault slipped contemporaneously, with slip terminating at similar times. Moment release occurred over about 3 s.

3.3. Relationship of Coseismic Slip to Aftershocks, Regional Seismicity, Pore Pressure Perturbations

Locations of aftershocks and analysis of regional seismicity suggest that the coseismic slip on the deeper part of the fault occurred at depths that are not commonly activated by regional seismicity. The majority of relocated aftershocks (Yeck et al., 2017) occurring within 5 km from the fault surface lie at depths of 5–7 km, with aftershock triggering slightly higher in the vicinity of the shallow slip patch (subevent 2; Figure 3a). Few aftershocks occurred below 8 km depth, and no aftershocks surround the areas of higher slip on the deeper parts of the fault. Aftershock distribution from the Pawnee earthquake differs from observations from other earthquakes, for which most aftershocks occur outside of the regions of high slip (e.g., Mendoza & Hartzell, 1988; Wetzler et al., 2018).

The aftershock depths, however, reflect the trend of regional induced seismicity. Ninety percent of earthquakes in central Oklahoma have hypocentral depths shallower than 6.8 km, and 99% of earthquakes have hypocentral depths shallower than 7.8 km (Figure S9; Rennolet et al., 2018). In contrast, the deeper rupture from our slip model occurs at depths of 9–10 km. Other rupture models (Fielding et al., 2017; Grandin et al., 2017; Pollitz et al., 2017) also indicate slip below 7 km depth (Text S1) and below the aftershock locations.

Comparisons of the distribution of on-fault pore fluid pressures with coseismic slip suggest a relationship between the rupture processes on the shallow fault ($<7 \text{ km}$) and pore pressures affected by fluid injection processes. Barbour et al. (2017) used coupled hydrologic-geomechanical models to compute the response of on-fault pore pressure from time-varying injection into local disposal wells for the Pawnee earthquake.

Estimates of pore pressure perturbations from immediately before the origin time (Figure 3a) suggest that the earthquake nucleated in a region of higher pore pressure perturbations (>15 kPa), that most slip on the shallow part of the fault occurred where the pore pressure perturbations were higher than 15 kPa, and that the deeper parts of the fault (and slip thereon) experienced minor to negligible changes in the pore pressures from fluid injection activities. Little slip occurred on the shallow parts of the fault (depths <7 km) outside of the zones of higher pore pressure perturbation. Intriguingly, the greatest depths of the aftershocks nearly corresponds with the greatest depths at which pore pressures are perturbed (5 kPa). Barbour et al. (2017) indicate that poroelastic effects were not significant on the deeper part of the fault.

4. Discussion and Conclusions

ASTFs and finite-fault inversion of regional and teleseismic P waveforms can be simultaneously explained by an M5.8 rupture that initiated with a 5.6-km-deep hypocenter and then proceeded to rupture distinct shallow and deeper parts of the fault. Rupture proceeded for about 3 s and can be modeled by a continuous rupture with a constant rupture speed of 2.7 km/s; rupture of the different parts of the fault do not require complex triggering mechanisms to explain the regional and teleseismic data. Although the seismic data did not permit greater spatial resolution of rupture speed, sensitivity studies indicate that the main features of the rupture model are not strongly affected by the parameters used in the inversions (see Text S3), and the finite-fault source complexity is supported by ASTF analyses that exhibit lesser dependence on parameter assumptions.

The absence of triggered aftershocks on the deeper part of the fault and the depth-distribution of regional seismicity suggest that the deeper fault may be stronger and further from critically stressed than shallower parts of the fault. Variations in fault strength may be explained by several mechanisms: (1) stress concentrations or reduced normal stresses due to coseismic effects, structural discontinuities, or initial/redistributed pore fluids (e.g., Manga et al., 2016; Nur & Booker, 1972; Pei et al., 2017; Pollitz et al., 2017); (2) aseismic response of parts of the fault (e.g., Barnhart et al., 2016; Chen et al., 2017; Guglielmi et al., 2015); or (3) that the deeper part of the fault is stronger than the shallower part of the fault, thereby inhibiting aftershock triggering and limiting the depth of seismicity, regionally. A reduction in the pore pressure changes with depth is one mechanism by which the shallower parts of the fault may be weakened relative to the deeper parts of the fault, and this mechanism may also explain the aftershock distribution and features of the earthquake rupture.

Recent dynamic rupture and fracture mechanical modeling of self-arresting ruptures (Galis et al., 2017) provide a mechanism to explain the rupture behavior of the Pawnee earthquake. These modeled ruptures initiate within zones where pore pressures are perturbed, and effective normal stresses are low, then propagate outside of the zones of high pore pressure perturbations, where they are arrested, due to increased fault strength. Seismicity and pore pressure modeling suggest differences in and explanations for the depth variations in fault strength, which may require the development of strong stress perturbations in the rupture front to promote rupture on the deeper parts of the fault (Barbour et al., 2017; Galis et al., 2017).

There is an intriguing correspondence between the rupture evolution of the Pawnee earthquake and that of the 2011 M5.7 Prague, Oklahoma, earthquake (Sun & Hartzell, 2014) that may suggest a class of failure mechanisms for induced earthquakes. The Prague earthquake also initiated near 5 km depth, followed by early, shallow moment release and then by rupture deeper on the fault. For the Pawnee earthquake, most of the seismic moment was released on the shallower part of the fault, though about one third of the total moment of the earthquake was released at greater depths. Stress drop from the Pawnee earthquake (4 MPa) is also comparable with what was found for the Prague earthquake (1.4 MPa), and it was previously noted that the stress drop differences reflect a difference in moment-area scaling: The areas of the faults participating in the ruptures of the Prague and Pawnee earthquakes are about 2.5–5 times larger than for the 2011 M5.8 Mineral, Virginia, earthquake, which has a comparable magnitude but a stress drop of 25 MPa (Hartzell et al., 2013; Sun & Hartzell, 2014). The vast majority of aftershocks from the Prague earthquake also locate at shallower depths (<7 km); however, some earthquakes occur at greater depths. Recent analyses by Lui and Huang (2019) also support the hypothesis that the source dynamics of moderate-sized induced earthquakes in Oklahoma are influenced by pore pressure distributions.

Our observations suggest that the Pawnee earthquake ruptured deeper parts of the fault than were triggered by aftershocks and at greater depths than most regional seismicity. Modeling results suggest that the earthquake rupture may have initiated within a zone of high pore pressure perturbations but then propagated outside of this zone. The potential for earthquakes to rupture outside of the zone of pore pressure perturbation is not accounted for by all models of induced earthquake maximum magnitudes (e.g., Eaton & Igonin, 2018; McGarr, 2014; Shapiro et al., 2010; van der Elst et al., 2016). Furthermore, Galis et al. (2017) note that these types of ruptures indicate a different scaling of maximum magnitude as a function of cumulative injected fluid volumes. Better understanding of the initial stresses, on-fault frictional conditions, and pore pressures within the fault zone will improve our understanding of the controls on earthquake physics and improve predictive models of the maximum magnitudes of induced earthquakes.

Acknowledgments

We thank Y. Huang, an anonymous reviewer, and editor L. Flesch for their helpful comments and efforts. The authors benefited from discussions and suggestions with W. Yeck, A. Barbour, K. Withers, D. Shelly, A. McGarr, D. McNamara, N. van der Elst, and P. Ampuero. A. Barbour provided pore pressure values. This work was supported by the U.S. Geological Survey Earthquake Hazards Program. Authors declare no competing interests. All data are available through the IRIS Data Management Center. The facilities of IRIS Data Services, and specifically the IRIS Data Management Center, were used for access to waveforms, related metadata, and/or derived products used in this study. IRIS Data Services are funded through the Seismological Facilities for the Advancement of Geoscience and EarthScope (SAGE) Proposal of the National Science Foundation under Cooperative Agreement EAR-1261681. The final slip model and earthquake catalog can be accessed from Moschetti et al. (2019; doi:10.5066/P91DWNMG). The finite-fault inversion code is available at online (<https://github.com/usgs/finite-fault>).

References

- Alt, R. C., & Zoback, M. D. (2016). In situ stress and active faulting in Oklahoma. *Bulletin of the Seismological Society of America*, 107(1), 216–228.
- Barbour, A. J., Norbeck, J. H., & Rubinstein, J. L. (2017). The effects of varying injection rates in Osage County, Oklahoma, on the 2016 Mw 5.8 Pawnee earthquake. *Seismological Research Letters*, 88(4), 1040–1053. <https://doi.org/10.1785/0220170003>
- Barnhart, W. D., Murray, J. R., Briggs, R. W., Gomez, F., Miles, C. P. J., Svarc, J., et al. (2016). Coseismic slip and early afterslip of the 2015 Illapel, Chile, earthquake: Implications for frictional heterogeneity and coastal uplift. *Journal of Geophysical Research: Solid Earth*, 121, 6172–6191. <https://doi.org/10.1002/2016JB013124>
- Chen, X., Nakata, N., Pennington, C., Haffener, J., Chang, J. C., He, X., et al. (2017). The Pawnee earthquake as a result of the interplay among injection, faults and foreshocks. *Scientific Reports*, 7(1), 4945. <https://doi.org/10.1038/s41598-017-04992-z>
- Clayton, P., Zalachoris, G., Rathje, E., Bheemasetti, T., Caballero, S., Yu, X., & Bennett, S. (2016). The geotechnical aspects of the September 3, 2016 Mw 5.8 Pawnee, Oklahoma earthquake. *GEER Association, Berkeley, California*, 10, G69885.
- Dziewonski, A. M., Chou, T. A., & Woodhouse, J. H. (1981). Determination of earthquake source parameters from waveform data for studies of global and regional seismicity. *Journal of Geophysical Research*, 86(B4), 2825–2852. <https://doi.org/10.1029/JB086iB04p02825>
- Eaton, D. W., & Igonin, N. (2018). What controls the maximum magnitude of injection-induced earthquakes? *The Leading Edge*, 37(2), 135–140. <https://doi.org/10.1190/tle37020135.1>
- Ekström, G., Nettles, M., & Dziewoński, A. M. (2012). The global CMT project 2004–2010: Centroid-moment tensors for 13,017 earthquakes. *Physics of the Earth and Planetary Interiors*, 200, 1–9.
- Ellsworth, W. L. (2013). Injection-induced earthquakes. *Science*, 341(6142), 1225942. <https://doi.org/10.1126/science.1225942>
- Fielding, E. J., Sangha, S. S., Bekaert, D. P., Samsonov, S. V., & Chang, J. C. (2017). Surface deformation of north-central Oklahoma related to the 2016 Mw 5.8 Pawnee earthquake from SAR interferometry time series. *Seismological Research Letters*, 88(4), 971–982. <https://doi.org/10.1785/0220170010>
- Galis, M., Ampuero, J. P., Mai, P. M., & Cappa, F. (2017). Induced seismicity provides insight into why earthquake ruptures stop. *Science Advances*, 3(12), eaap7528. <https://doi.org/10.1126/sciadv.aap7528>
- Grandin, R., Vallée, M., & Lacassin, R. (2017). Rupture process of the Mw 5.8 Pawnee, Oklahoma, earthquake from Sentinel-1 InSAR and seismological data. *Seismological Research Letters*, 88, 994–1004. <https://doi.org/10.1785/0220160226>
- Guglielmi, Y., Cappa, F., Avouac, J. P., Henry, P., & Elsworth, D. (2015). Seismicity triggered by fluid injection-induced aseismic slip. *Science*, 348(6240), 1224–1226. <https://doi.org/10.1126/science.aab0476>
- Hansen, P. C. (2005). *Rank-deficient and discrete ill-posed problems: Numerical aspects of linear inversion* (Vol. 4). Philadelphia, PA: SIAM Monographs on Mathematical Modeling and Computation.
- Hartzell, S., Mendoza, C., & Zeng, Y. (2013). Rupture model of the 2011 Mineral, Virginia, earthquake from teleseismic and regional waveforms. *Geophysical Research Letters*, 40, 5665–5670. <https://doi.org/10.1002/2013GL057880>
- Hartzell, S. H. (1978). Earthquake aftershocks as Green's functions. *Geophysical Research Letters*, 5(1), 1–4. <https://doi.org/10.1029/GL005i001p00001>
- Hartzell, S. H., & Heaton, T. H. (1983). Inversion of strong ground motion and teleseismic waveform data for the fault rupture history of the 1979 Imperial Valley, California, earthquake. *Bulletin of the Seismological Society of America*, 73(6A), 1553–1583.
- Healy, J. H., Hamilton, R. M., & Raleigh, C. B. (1970). Earthquakes induced by fluid injection and explosion. *Tectonophysics*, 9(2–3), 205–214. [https://doi.org/10.1016/0040-1951\(70\)90017-X](https://doi.org/10.1016/0040-1951(70)90017-X)
- Helmberger, D. V. (1983). Theory and application of synthetic seismograms. In H. Kanamori & E. Boschi (Eds.), *Earthquakes: observation theory and interpretation* (pp. 174–222). Amsterdam: North-Holland Publishing Company.
- Herrmann, R. B., Benz, H., & Ammon, C. J. (2011). Monitoring the earthquake source process in North America. *Bulletin of the Seismological Society of America*, 101(6), 2609–2625. <https://doi.org/10.1785/0120110095>
- Keranen, K. M., Weingarten, M., Abers, G. A., Bekins, B. A., & Ge, S. (2014). Sharp increase in central Oklahoma seismicity since 2008 induced by massive wastewater injection. *Science*, 345(6195), 448–451. <https://doi.org/10.1126/science.1255802>
- Lawson, C. L., & Hanson, R. J. (1974). *Solving least squares problems*. Upper Saddle River, NJ: Prentice-Hall, Inc.
- Ligorria, J. P., & Ammon, C. J. (1999). Iterative deconvolution and receiver-function estimation. *Bulletin of the Seismological Society of America*, 89(5), 1395–1400.
- Liu, P.-C., Hartzell, S., & Stephenson, W. (1995). Non-linear multiparameter inversion using a hybrid global search algorithm: Applications in reflection seismology. *Geophysical Journal International*, 122, 991–1000. <https://doi.org/10.1111/j.1365-246X.1995.tb06851.x>
- Llenos, A. L., & Michael, A. J. (2013). Modeling earthquake rate changes in Oklahoma and Arkansas: Possible signatures of induced seismicity. *Bulletin of the Seismological Society of America*, 103(5), 2850–2861. <https://doi.org/10.1785/0120130017>
- López-Comino, J. A., & Cesca, S. (2018). Source complexity of an injection induced event: The 2016 Mw 5.1 Fairview, Oklahoma earthquake. *Geophysical Research Letters*, 45, 4025–4032. <https://doi.org/10.1029/2018GL077631>
- Lui, S. K. Y., & Huang, Y. (2019). Do injection-induced earthquakes rupture away from injection wells due to fluid pressure change? *Bulletin of the Seismological Society of America*, 109, 358–371. <https://doi.org/10.1785/0120180233>

- Manga, M., Wang, C. Y., & Shirzaei, M. (2016). Increased stream discharge after the 3 September 2016 Mw 5.8 Pawnee, Oklahoma earthquake. *Geophysical Research Letters*, 43, 11,588–11,594. <https://doi.org/10.1002/2016GL071268>
- McGarr, A. (2014). Maximum magnitude earthquakes induced by fluid injection. *Journal of Geophysical Research: Solid Earth*, 119, 1008–1019. <https://doi.org/10.1002/2013JB010597>
- McGarr, A., & Barbour, A. J. (2017). Wastewater disposal and the earthquake sequences during 2016 near Fairview, Pawnee, and Cushing, Oklahoma. *Geophysical Research Letters*, 44, 9330–9336. <https://doi.org/10.1002/2017GL075258>
- Mendoza, C., & Hartzell, S. (2013). Finite-fault source inversion using teleseismic *P* waves: Simple parameterization and rapid analysis. *Bulletin of the Seismological Society of America*, 103(2A), 834–844. <https://doi.org/10.1785/0120120069>
- Mendoza, C., & Hartzell, S. H. (1988). Aftershock patterns and main shock faulting. *Bulletin of the Seismological Society of America*, 78(4), 1438–1449.
- Moschetti, M. P., Hartzell, S. H., & Herrmann, R. B. (2019). Data for rupture model of the 2016 M5.8 Pawnee, Oklahoma earthquake: U.S. Geological Survey data release. <https://doi.org/10.5066/P91DWNMG>
- Moschetti, M. P., Hoover, S. M., & Mueller, C. S. (2016). Likelihood testing of seismicity-based rate forecasts of induced earthquakes in Oklahoma and Kansas. *Geophysical Research Letters*, 43, 4913–4921. <https://doi.org/10.1002/2016GL068948>
- Nur, A., & Booker, J. R. (1972). Aftershocks caused by pore fluid flow? *Science*, 175(4024), 885–887. <https://doi.org/10.1126/science.175.4024.885>
- Okada, Y. (1985). Surface deformation due to shear and tensile faults in a half-space. *Bulletin of the Seismological Society of America*, 75(4), 1135–1154.
- Pei, S., Peng, Z., & Chen, X. (2017). Locations of injection-induced earthquakes in Oklahoma controlled by crustal structures. *Journal of Geophysical Research: Solid Earth*, 123, 2332–2344. <https://doi.org/10.1002/2017JB014983>
- Petersen, M. D., Mueller, C. S., Moschetti, M. P., Hoover, S. M., Llenos, A. L., Ellsworth, W. L., et al. (2016). Seismic-hazard forecast for 2016 including induced and natural earthquakes in the central and eastern United States. *Seismological Research Letters*, 87(6), 1327–1341. <https://doi.org/10.1785/0220160072>
- Petersen, M. D., Mueller, C. S., Moschetti, M. P., Hoover, S. M., Rukstales, K. S., McNamara, D. E., et al. (2018). 2018 one-year seismic hazard forecast for the central and eastern United States from induced and natural earthquakes. *Seismological Research Letters*, 89(3), 1049–1061. <https://doi.org/10.1785/0220180005>
- Petersen, M. D., Mueller, C. S., Moschetti, M. P., Hoover, S. M., Shumway, A. M., McNamara, D. E., et al. (2017). 2017 one-year seismic hazard forecast for the central and eastern United States from induced and natural earthquakes. *Seismological Research Letters*, 88(3), 772–783. <https://doi.org/10.1785/0220170005>
- Politz, F. F., Wicks, C., Schoenball, M., Ellsworth, W., & Murray, M. (2017). Geodetic slip model of the 3 September 2016 Mw 5.8 Pawnee, Oklahoma, earthquake: Evidence for fault-zone collapse. *Seismological Research Letters*, 88(4), 983–993. <https://doi.org/10.1785/0220170002>
- Raleigh, C. B., Healy, J. H., & Bredehoeft, J. D. (1976). An experiment in earthquake control at Rangely, Colorado. *Science*, 191(4233), 1230–1237. <https://doi.org/10.1126/science.191.4233.1230>
- Rennolet, S. B., Moschetti, M. P., Thompson, E. M., & Yeck, W. L. (2018). A flatfile of ground motion intensity measurements from induced earthquakes in Oklahoma and Kansas. *Earthquake Spectra*, 34(1), 1–20. <https://doi.org/10.1193/101916EQS175DP>
- Segall, P., & Lu, S. (2015). Injection-induced seismicity: Poroelastic and earthquake nucleation effects. *Journal of Geophysical Research: Solid Earth*, 120, 5082–5103. <https://doi.org/10.1002/2015JB012060>
- Shapiro, S. A., Dinske, C., Langenbruch, C., & Wenzel, F. (2010). Seismogenic index and magnitude probability of earthquakes induced during reservoir fluid stimulations. *The Leading Edge*, 29(3), 304–309. <https://doi.org/10.1190/1.3353727>
- Somerville, P., Irikura, K., Graves, R., Sawada, S., Wald, D., Abrahamson, N., et al. (1999). Characterizing crustal earthquake slip models for the prediction of strong ground motion. *Seismological Research Letters*, 70(1), 59–80. <https://doi.org/10.1785/gssrl.70.1.59>
- Sun, X., & Hartzell, S. (2014). Finite-fault slip model of the 2011 Mw 5.6 Prague, Oklahoma earthquake from regional waveforms. *Geophysical Research Letters*, 41, 4207–4213. <https://doi.org/10.1002/2014GL060410>
- U.S. Geological Survey (2016). Regional moment tensor for M 5.8, 14km NW of Pawnee, Oklahoma. Retrieved from https://earthquake.usgs.gov/earthquakes/eventpage/us10006jxs/moment-tensor?source=us&code=us_10006jxs_mwr, (last accessed December 21, 2018).
- U.S. Geological Survey (2018). Population exposure to strong ground shaking, MMI VI+: <https://earthquake.usgs.gov/earthquakes/eventpage/us10006jxs#pager>, (last accessed, December 21, 2018).
- van der Elst, N. J., Page, M. T., Weiser, D. A., Goebel, T. H., & Hosseini, S. M. (2016). Induced earthquake magnitudes are as large as (statistically) expected. *Journal of Geophysical Research: Solid Earth*, 121, 4575–4590. <https://doi.org/10.1002/2016JB012818>
- Weingarten, M., Ge, S., Godt, J. W., Bekins, B. A., & Rubinstein, J. L. (2015). High-rate injection is associated with the increase in US mid-continent seismicity. *Science*, 348(6241), 1336–1340. <https://doi.org/10.1126/science.aab1345>
- Wetzler, N., Lay, T., Brodsky, E. E., & Kanamori, H. (2018). Systematic deficiency of aftershocks in areas of high coseismic slip for large subduction zone earthquakes. *Science Advances*, 4(2), eaao3225. <https://doi.org/10.1126/sciadv.aao3225>
- Yeck, W. L., Hayes, G. P., McNamara, D. E., Rubinstein, J. L., Barnhart, W. D., Earle, P. S., & Benz, H. M. (2017). Oklahoma experiences largest earthquake during ongoing regional wastewater injection hazard mitigation efforts. *Geophysical Research Letters*, 44, 711–717. <https://doi.org/10.1002/2016GL071685>